Efficient Mercury Removal from Aqueous Solutions Using Carboxylated $Ti_3C_2T_x$ MXene

Ali Pournaghshband Isfahani[1†], Ahmad A. Shamsabadi[1†],
Farbod Alimohammadi[2], and Masoud Soroush[1*]

[1]Department of Chemical and Biological Engineering, Drexel University, Philadelphia, Pennsylvania 19104, United States

[2]Department of Chemistry, Temple University, Philadelphia, Pennsylvania 19122, United States

March 14, 2022

Revised Version

Submitted for Publication in *Journal of Hazardous Materials*

Keywords: Mercury-ion removal, adsorption, degradation, $Ti_3C_2T_x$, carboxylation.

[†]*These authors contributed equally to this work.*

[*] *Corresponding author, Tel: +1-215-895-1710; E-mail: soroushm@drexel.edu*

Abstract

Water supplies contaminated with heavy metals are a worldwide concern. MXenes have properties that make them attractive for the removal of metal ions from water. This work presents a simple one-step method of $Ti_3C_2T_x$ carboxylation that involves the use of a chelating agent with a linear structure, providing strong carboxylic acid groups with high mobility. The carboxylation decreases the zeta-potential of $Ti_3C_2T_x$ by ~16 to ~18 mV over a pH range of 2.0 to 8.5, and improves $Ti_3C_2T_x$ stability in the presence of molecular oxygen. pH in the range of 2–6 has a negligible effect on the adsorption capacity of $Ti_3C_2T_x$ and COOH–$Ti_3C_2T_x$. Compared to $Ti_3C_2T_x$, COOH–$Ti_3C_2T_x$ has a slightly higher but much faster mercury uptake, and the concentration of mercury ions leached out from it is lower. For both $Ti_3C_2T_x$ and COOH–$Ti_3C_2T_x$, the leached mercury ion concentration is far below the US-EPA maximum level. At an initial Hg^{2+} concentration of 50 ppm and pH of 6, COOH–$Ti_3C_2T_x$ has the equilibrium adsorption capacity of 499.7 mg/g and removes 95% of Hg^{2+} in less than 1 min. Moreover, it has an equilibrium time of 5 min, significantly shorter than that of $Ti_3C_2T_x$ (~ 60 min). Finally, its mercury-ion uptake capacity is higher than commercially available adsorbents reported in the literature. Its mercury removal is mainly via chemisorption and monolayer adsorption.

1. Introduction

The presence of heavy metal ions (HMIs) in aquatic systems, particularly in drinking water, is of growing global concern [1-3]. Among heavy metals, mercury (Hg), which has many industrial applications, is a hazardous water pollutant that can damage the nervous system. The U.S. Environmental Protection Agency (EPA) has placed an upper limit of 2 ppb for Hg ions in water and wastewater streams [4]. Conventional methods for the removal of heavy metals are precipitation, electrolysis, ion exchange, adsorption [5], membranes, concentration and solvent extraction. Among them, adsorption has received considerable attention for its considerable removal efficiency, low cost, and inherent flexibility [6, 7].

Traditional sorbents such as activated carbons, clays, and zeolites are not efficient for water remediation due to their weak affinity with most metal ions, low surface area, and pH instability [8, 9]. Although metal-organic frameworks (MOFs) have demonstrated exceptional capacity to adsorb heavy metal ions and water contaminants, their applications have been limited due to their severe agglomeration, low stability, and complex synthesis [10]. In contrast, two-dimensional (2D) materials with special structural features and abundant functional groups can be ideal candidates for the removal of heavy metal ions from wastewater effluents. Graphene oxide (GO), molybdenum disulfide (MoS_2), and their derivative are attractive for the adsorption of metal ions from wastewater. The particular structures and excellent affinity of different functional groups on sorbents (e.g., carboxyl, hydroxyl, and carbonyl) towards metal ions are their advantages [11, 12]. The selectivity and capacity of the adsorbents can be improved by surface modification with different chemical compounds (e.g., dithiocarbamate, polyethyleneimine (PEI), polyacrylamide, polymaleicamide dendrimer) and functional groups. The electron-donating property of most dendrimers forms Hg-complexes, which enhance the mercury-ion removal capacity of modified

GO nanosheets. It was reported that more than 99% Hg^{2+} was removed by anchoring SnS_2 on GO nanosheets [13]. The modification of GO with thiol groups also resulted in a six-fold higher Hg^{2+} uptake than the pristine GO [14]. The synergistic effect of three adsorption mechanisms, the soft Lewis acid-base and electrostatic interactions of S^{2-} with mercury ions, and the electrostatic interactions and ion-exchange capability of –OH and –COOH groups with Hg^{2+}, are the main reasons for high-efficient removal of thiol-modified GO nanosheets. Additionally, the weak stability of GO in acidic and alkaline environments and difficulty in the separation of GO particles from effluent are the main obstacles to their practical applications. Moreover, it has also been reported that GO nanosheets have moderate toxicity to human cells [15, 16]. However, in the case of MoS_2 nanomaterials, poor dispersibility in aqueous media and small interlayer spacing of ~2.7 Å limit their application for heavy metal removal [17, 18].

2D structure, hydrophilicity, and tunability of MXenes have provided potential alternatives for the removal of mercury ions from aqueous solutions [19]. Yu *et al.* [20] recently reviewed the application of MXenes and functionalized MXenes for the removal of different water pollutants and heavy metal ions, highlighting that the removal efficiency strongly depends on the functional groups on the MXene and the chemistry of the contaminants. MXenes possess abundant active sites (−OH, –F, and −O), negative zeta potential (pH ≥ 2.3), and excellent dispersity in water, which can facilitate mercury capture [21-31]. The in-situ reductive-adsorptive feature of MXenes is distinctive and makes them very appropriate for the removal of metal ions from wastewater. $Ti_3C_2T_x$ was utilized for the selective adsorption-reduction of BrO_3^- to Br^- in aqueous waste streams [32]. For example, Cr^{6+} ions were reduced to less toxic Cr^{3+} and then removed by $Ti_3C_2T_x$ nanosheets. Reductive adsorption of Cu^{2+} was reported for both delaminated and multi-layered MXene nanosheets. However, $Ti_3C_2T_x$ decomposes to TiO_2 crystals in aqueous media due to

surface oxidation [33-35]. The low energy formation of OH-terminated $Ti_3C_2T_x$ supports faster oxidation of this material in aqueous media. Hu *et al.* [36] studied the removal of Hg^{2+} from mixed divalent cationic metal solutions using $Ti_3C_2T_x$. They ascribed the good selectivity of the adsorbent to its large number of oxygen-containing functional groups on its surface. They reported that the adsorbent maintains a high adsorption capacity at low pH. Shahzad *et al.* [37] studied the Hg^{2+} removal capacity of $Ti_3C_2T_x$ and Ti_3CNT_x (titanium carbonitride) MXenes from aqueous solutions. Their study confirmed the interaction of bimetal and hydroxyl groups with Hg^{2+} via electrostatic interactions and adsorption-coupled reduction. Their batch adsorption studies showed that $Ti_3C_2T_x$ and Ti_3CN have Hg^{2+} removal capacities of 5473 and 4606 mg/g, respectively. A nice critical review by Othman et al. [38] has put MXenes adsorption behavior toward heavy metals into perspective.

The functionalization of $Ti_3C_2T_x$ surface to delay the degradation and improve the rate of adsorption has been investigated. For example, carboxylated $Ti_3C_2T_x$ MXene (core-shell COOH-MXene@PEI-PAA) synthesized via the layer-by-layer self-assembly method showed good stability and reusability for dye removal [39]. The presence of positively-charged groups in the nanocomposite decreases its capacity for metal ions capture. MXenes functionalized with MoS_2 displayed a high mercury adsorption capacity of 7.16 mmol/g and a distribution coefficient of 7.87×10^5 mL/g [40]. Other groups that have reported the carboxylation of $Ti_3C_2T_x$ and its potential for heavy-metal ion removal are our group [41] and Zhang *et al.* [42]. Laki *et al.* [41] modified $Ti_3C_2T_x$ with a chloroacetic acid solution at room temperature and prepared carboxylated $Ti_3C_2T_x$ ($Ti_3C_2T_x$–COOH). Their $Ti_3C_2T_x$–COOH showed high stability and dispersity in aqueous media and negative zeta potential in a wide range of pH. Zhang *et al.* [42] reported that: their synthesized carboxyl functionalized $Ti_3C_2T_x$ (via the attachment of phenyl carboxylic acid to $Ti_3C_2T_x$ via a

three-step reaction) had significantly higher stability in water than the pristine $Ti_3C_2T_x$; and it exhibited superior U(VI) and Eu(III) adsorption capacities up to 334.8 mg/g and 97.1 mg/g, respectively. It is believed that the carboxyl groups stabilize MXene layers, owing to higher energy formation compared to the OH–terminated $Ti_3C_2T_x$ [43]. However, bonding the carboxyl group directly to a benzene ring in the benzene carboxylic acid (benzoic acid) makes this acid weak ($K_a = 6.4 \times 10^{-5}$ at 25°C). Moreover, the benzene ring restricts the mobility of the carboxylic group and thereby decreases its availability for efficient metal ions capture.

In this study, we present a simple one-step method of $Ti_3C_2T_x$ carboxylation that involves the use of a chelating agent with a linear structure, providing strong carboxylic acid groups with high mobility. It investigates how introducing carboxyl functional groups on the surface of $Ti_3C_2T_x$ MXene affects the ability of $Ti_3C_2T_x$ to adsorb mercury and mitigates $Ti_3C_2T_x$ oxidation without sacrificing the dispersibility and hydrophilicity of the MXene. The surface and structural properties of the carboxylated $Ti_3C_2T_x$ (COOH–$Ti_3C_2T_x$) are studied using Fourier transform infrared (FTIR) and UV-Vis spectroscopies, zeta-potential measurements, scanning electron microscopy (SEM), and X-ray diffraction (XRD) analyses. The mercury adsorption of the surface-modified MXene (COOH–$Ti_3C_2T_x$) is studied in a batch system at different pH values and with different initial conditions, and likely adsorption mechanisms are discussed. Preliminary results from this study had been presented at the 2019 AIChE Annual Conference [41].

2. Materials and Methods

2.1. Materials

Mercury (II) nitrate hydrate (>98%) and chloroacetic acid (>99%) were purchased from Bean Town Chemical (BTC). Nitric acid (>69.1%) and sodium hydroxide (>98%) were bought from Fishers scientific. Hydrochloric acid (HCl>37%), hydrofluoric acid (HF>51%), and lithium

chloride (LiCl > 99%) were supplied from Sigma-Aldrich Co. Diphenylthiocarbazone (dithizone), and distilled 1,4-dioxane were obtained from TCI, Inc. Thiourea was purchased from Alfa Aesar; it was used for MXene recovery. Deionized water was purchased from Hanna Instruments (HI-70436 De-Ionized water). A stock solution containing 1000 $mg \cdot L^{-1}$ of Hg^{2+} was prepared by dissolving Hg $(NO_3)_2$ in deionized water acidified with HNO_3 (0.5% v/v) to prevent hydrolysis. All solutions and reagents for spectrophotometric determination of trace levels of mercury(II) were prepared according to the procedure reported in [44].

2.2 Synthesis of $Ti_3C_2T_x$ and COOH–$Ti_3C_2T_x$

Ti_3AlC_2, MAX phase was prepared according to the literature [45]. Delaminated $Ti_3C_2T_x$ was synthesized by selective etching of the Al element from the Ti_3AlC_2 MAX phase by using a diluted HF/HCl solution [46]. 2 mL HF solution and 12 mL HCl (38% v/v) were added to 6 mL deionized water in a polypropylene vial. 1 g Ti_3AlC_2 powder was added slowly to the solution and stirred (300 rpm) for 24 h at 35ºC. After the etching process, the excess acids were removed via centrifugation (3500 rpm, 10 min) and washing the collected solid several times with water to attain a pH between 5-6. Next, 50 mL of DI water was added to the collected solid, followed by adding 1 g of lithium chloride to the mixture and stirring it for 24 h at 35ºC to delaminate $Ti_3C_2T_x$ [47]. The colloidal solution was washed and centrifuged at 3500 rpm for 10 min to remove the excess amount of lithium ions. The sediments were shaken and vortexed in water and centrifuged at 3500 rpm. The supernatant was collected as the high quality MXene intercalated with Li^+ [48] for further use, and this process was repeated a few more times. The collected supernatant colloidal solution was placed in an argon-sealed vial [49], and its concentration was measured using the gravimetric method at room temperature. The COOH–$Ti_3C_2T_x$ was prepared by the addition of 1.7 g chloroacetic acid to a 1 mg/mL delaminated $Ti_3C_2T_x$ colloidal solution at 0 ºC and stirred for 2h

to convert –OH groups on the surface of $Ti_3C_2T_x$ into carboxyl groups (Figure 1). The mixture was then neutralized with an abundant amount of distilled water to obtain a pH value of ~5.5 for the supernatant.

2.3. Batch Adsorption Experiments

We measured trace levels (0.1–500 ppm) of mercury (II) spectrophotometrically using an ultraviolet-visible (UV-Vis) spectrometer. The calibration of the spectrometer involved the following steps. 0.8 mL of a 0.2 mM dithizone solution and 0.1 mL of 1M H_2SO_4 were first added to 4.1 mg of a 0.1–500 ppm mercury solution. 5 mL dioxane was then added to the mixture. For

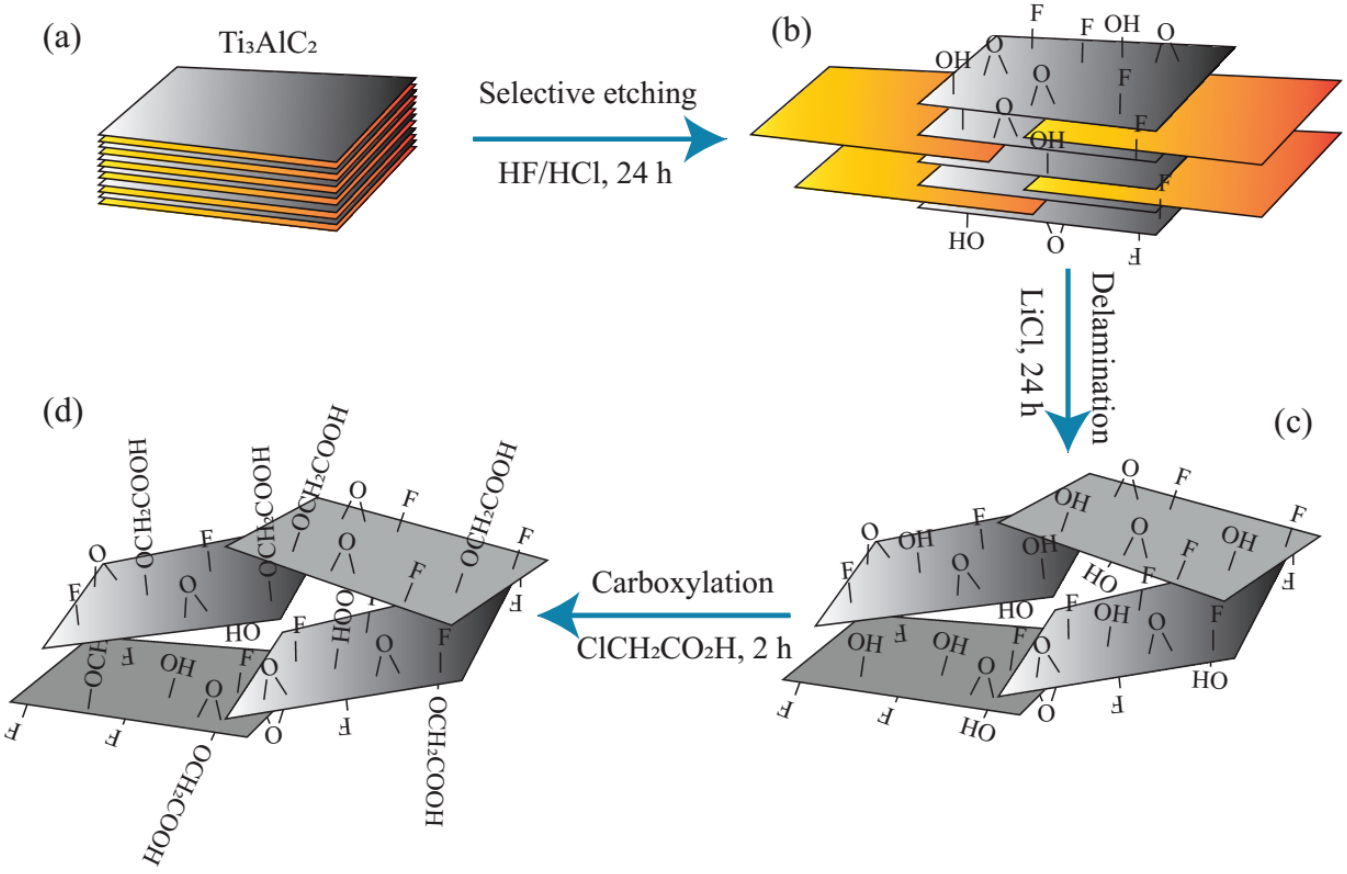

Figure 1. Schematic representation of the COOH−$Ti_3C_2T_x$ preparation. (a) MAX phase, (b) un-delaminated $Ti_3C_2T_x$, (c) delaminated $Ti_3C_2T_x$, and (d) COOH−$Ti_3C_2T_x$.

Hg^{2+} concentrations in the range of 0.1–50 ppm, a linear correlation between the absorbance and Hg^{2+} concentration was obtained.

The mercury adsorption experiments of the $Ti_3C_2T_x$ and COOH–$Ti_3C_2T_x$ were conducted using a batch method (V/m of 10 and 100 mL/mg). 1–1000 ppm Hg^{2+} aqueous solutions were prepared. 1 mg of COOH–$Ti_3C_2T_x$ or $Ti_3C_2T_x$ was added to 10 mL of an Hg^{2+} aqueous solution and stirred slowly for 24 h at 25°C to reach adsorption equilibrium. Next, the mixture was centrifuged (at 3500 rpm and for 10 min) and filtered using a 25 mm hydrophilic PTFE (0.22 μm) filter with no mercury ions adsorption. The supernatant solution was collected to determine Hg^{2+} content of the sample via UV-Vis spectroscopy. The Hg^{2+} concentration of each solution was measured before and after adsorption. Using these concentrations and the following equations, we calculated the adsorption capacity (Q_t, mg/g) and the mercury removal percentage (%):

$$Q_t = \frac{C_0 V - C_t V}{m} \quad (1)$$

$$\text{Removal (\%)} = \frac{C_0 - C_t}{C_0} \times 100 \quad (2)$$

where m (g) is the mass of the adsorbent, V (mL) is the volume of the solution, and C_0 and C_t (mg/mL) are the Hg^{2+} concentration of the solution before and after the adsorption, respectively. Each COOH–$Ti_3C_2T_x$ adsorbent was recovered by centrifugation and desorbed in 50 mL of an acidic mixture of nitric acid (0.5 M) and thiourea (5 wt.%.) stirred at 200 rpm and 298 K for 8 h.

2.4. Effect of pH on Adsorption Capacity

To study the effect of pH on the adsorption capacity, we conducted the batch adsorption experiments (V/m = 100 mL/mg) with initial Hg concentrations of 50 and 200 ppm at the pH range of 2–6. The pH of the system was controlled by adding 0.1 M HNO_3. We carefully monitored pH to ensure that it remained constant during the tests.

2.5. Hg Leaching Test

To simulate the potential mercury contamination during the adsorbent disposal in a landfill, a chemical analysis (namely, toxicity characteristic leaching procedure) was conducted. First, the Hg–$Ti_3C_2T_x$ and Hg–COOH–$Ti_3C_2T_x$ samples from the adsorption experiments were dried at room temperature. 5 mg of each sample was then added to 100 mL of an extractant solution (0.57 vol.% glacial acetic acid) and stirred at 100 rpm and room temperature. The solution was filtered, and the mercury concentration was measured using the UV-vis absorption method at different extraction time instants.

2.6. Characterization Methods

$Ti_3C_2T_x$, COOH– $Ti_3C_2T_x$, and COOH– $Ti_3C_2T_x$–Hg complexes were characterized using multiple techniques to evaluate their morphology and physicochemical properties. Zeta-potential (ζ-potential) was measured using dynamic light-scattering analysis (Brookhaven Instrument Corp., Holtsville, New York) at room temperature. X-ray diffraction (XRD) patterns were recorded using an X-ray diffractometer (Rigaku SmartLab, Akishima-shi, Tokyo, Japan) with Cu Kα radiation (λ = 0.15406 nm), 0.02° step size, and dwelling time of 0.5 s. Transmission electron microscopy (TEM) images were obtained using a JEOL JEM-1400 series 120kV Transmission Electron Microscope (Peabody, Massachusetts, USA). In addition, a Zeiss Supra 50VP scanning electron microscopy (SEM) and energy dispersive X-ray analysis (EDX) were conducted to check the morphology and elemental composition. Fourier transform infrared (FTIR) spectra were obtained on a Thermo Fisher Nicolet IS50 FTIR spectrometer (Thermo Fisher Scientific, MA, USA) in the wavenumber range of 3600–600 cm^{-1} with the resolution of 0.5 cm^{-1}. UV–Vis was conducted using a UV–1700 Shimadzu spectrophotometer (Shimadzu, Kyoto, Japan) with a 10 mm optical path length cuvette and scanning from 200 to 1000 nm. Thermogravimetric analysis (TGA) was

performed using a SDT 650 (TA Instruments, Utah USA) between 50 to 750 °C with enhancement rate of 20 °C·min^{-1} under highly pure nitrogen.

3. Results and Discussion

3.1. Characterization of $Ti_3C_2T_x$ and COOH–$Ti_3C_2T_x$

TEM analysis shown in Figures S1a and S1b (in the Supplementary Information) indicates that the functionalization does not alter the morphology of the flakes. Figure S1c depicts the ζ–potential of $Ti_3C_2T_x$ and COOH–$Ti_3C_2T_x$ colloidal solutions (~0.04 mg·mL^{-1}) in the pH range of 2.0 to 8.5. The ζ-potential of COOH– $Ti_3C_2T_x$ at a pH value of 5.5 is –44.3 mV, which is almost twice that of $Ti_3C_2T_x$, confirming the successful carboxylation of $Ti_3C_2T_x$. It seems that replacing the hydroxyl groups that each has one oxygen atom with the carboxyl group that each has two oxygen atoms is responsible for this improvement. Moreover, carboxyl anions are very stable due to the resonance, which improves the adsorption capacity of COOH–$Ti_3C_2T_x$ by preventing aggregation of the nanosheets. FTIR spectra demonstrate the successful replacement of –OH groups with –COOH moieties after the modification. As can be seen in Figure S1d, characteristic peaks of COOH–$Ti_3C_2T_x$ appeared at 700−900, 1375, 1750, and 2150–2280 cm^{-1}. The absorption peak at 597 cm^{-1} is related to the vibration of Ti–O bonds [22, 50]. The new peaks at 1750, 1400, and 1200 cm^{-1} correspond to the carbonyl linkages, confirming the modification of $Ti_3C_2T_x$.

To determine the extent of the $Ti_3C_2T_x$ modification, we performed TGA on $Ti_3C_2T_x$ and COOH–$Ti_3C_2T_x$ (Figure 2a). After complete decomposition, the residual Ti_3C_2 in the $Ti_3C_2T_x$ and in COOH–$Ti_3C_2T_x$ samples (denoted by X_{MX} and $X_{COOH-MX}$) were 89 and 84 wt. %, respectively. COOH–$Ti_3C_2T_x$ showed more weight loss than $Ti_3C_2T_x$ due to the presence of the organic CH_2COOH groups [51, 52]. From these values, the grafting degree (GD), the number of –CH_2COOH groups grafted onto each $Ti_3C_2T_x$ repeat unit, can be calculated using the equation [53]:

$$GD = \left(\frac{X_{MX} - X_{COOH-MX}}{M_{CH_2COOH}}\right)\left(\frac{X_{COOH-MX}}{M_{Ti_3C_2T_x}}\right)^{-1} \quad (3)$$

where $M_{Ti_3C_2T_x}$ and M_{CH_2COOH} are the molar masses of a $Ti_3C_2T_x$ repeat unit and CH_2COOH, respectively. Assuming that $x = 2$ (T= –O, –OH, –F), and for every –OH group on the surface of the MXene, there are three –F and –O functional groups (that is, the molar fraction of –OH groups among all pristine-MXene functional groups is 0.25), $M_{Ti_3C_2T_x} = 201.65\ g/mol$. $M_{CH_2COOH} = 59.05$. Thus, our sample has a $GD \approx 0.20$, which implies that 20 –OCH_2COOH groups were grafted to every 100 $Ti_3C_2T_x$ repeat units. The grafting yield (G_y), the fraction of the –OH groups that participated in the grafting, can be calculated using [53]:

$$G_{OH} = \frac{GD}{y_{OH}\, x} \quad (4)$$

where y_{OH} is the molar fraction of the –OH groups among all pristine-MXene functional groups. $y_{OH} = 0.25$, $x = 2$, and $G_{OH} = 0.40$ suggest that about 40% of –OH groups on $Ti_3C_2T_x$ were converted to –OCH_2COOH. The partial conversion of the OH groups can be due to the incomplete delamination of the $Ti_3C_2T_x$ sample, which limits the accessibility of all reactive groups to $ClCH_2COOH$.

XRD measurements (Figure 2b) indicate that the characteristic peaks of (002), (004) and (008) at 2θ = 6.5°, 14° and 27°, respectively, confirming the successful synthesis of $Ti_3C_2T_x$. The sharp (002) peak was shifted to lower frequencies at 2θ = 4.7°, indicating a larger d-spacing layer ~19.2 Å for COOH–$Ti_3C_2T_x$ and successful carboxylation of $Ti_3C_2T_x$ surfaces. After mercury adsorption by $Ti_3C_2T_x$ and COOH–$Ti_3C_2T_x$, a small peak at 2θ = 35° appeared, suggesting a small portion of Ti atoms oxidized into TiO_2 during the reduction of Hg^{2+} to Hg^{+} and Hg^{0}. This is a well-known mechanism of metal adsorption by MXenes [54]. The lower intensity of the TiO_2 peak for the COOH–$Ti_3C_2T_x$ samples verifies more stability of the modified MXene against oxidation. The

(002) peak of the pristine $Ti_3C_2T_x$ shifted from 6.3° to 5.7° (d-spacing from 14 Å to 15.5 Å), indicating that the intercalation of mercury ions expanded the MXene interlayer spacing [23, 55]. However, the (002) peak of COOH–$Ti_3C_2T_x$ after mercury adsorption slightly shifted to a higher angle, which explains the smaller interlayer spacing. The contradiction in the trend can be attributed to the stronger interactions between the carboxylic acid groups and the mercury ions

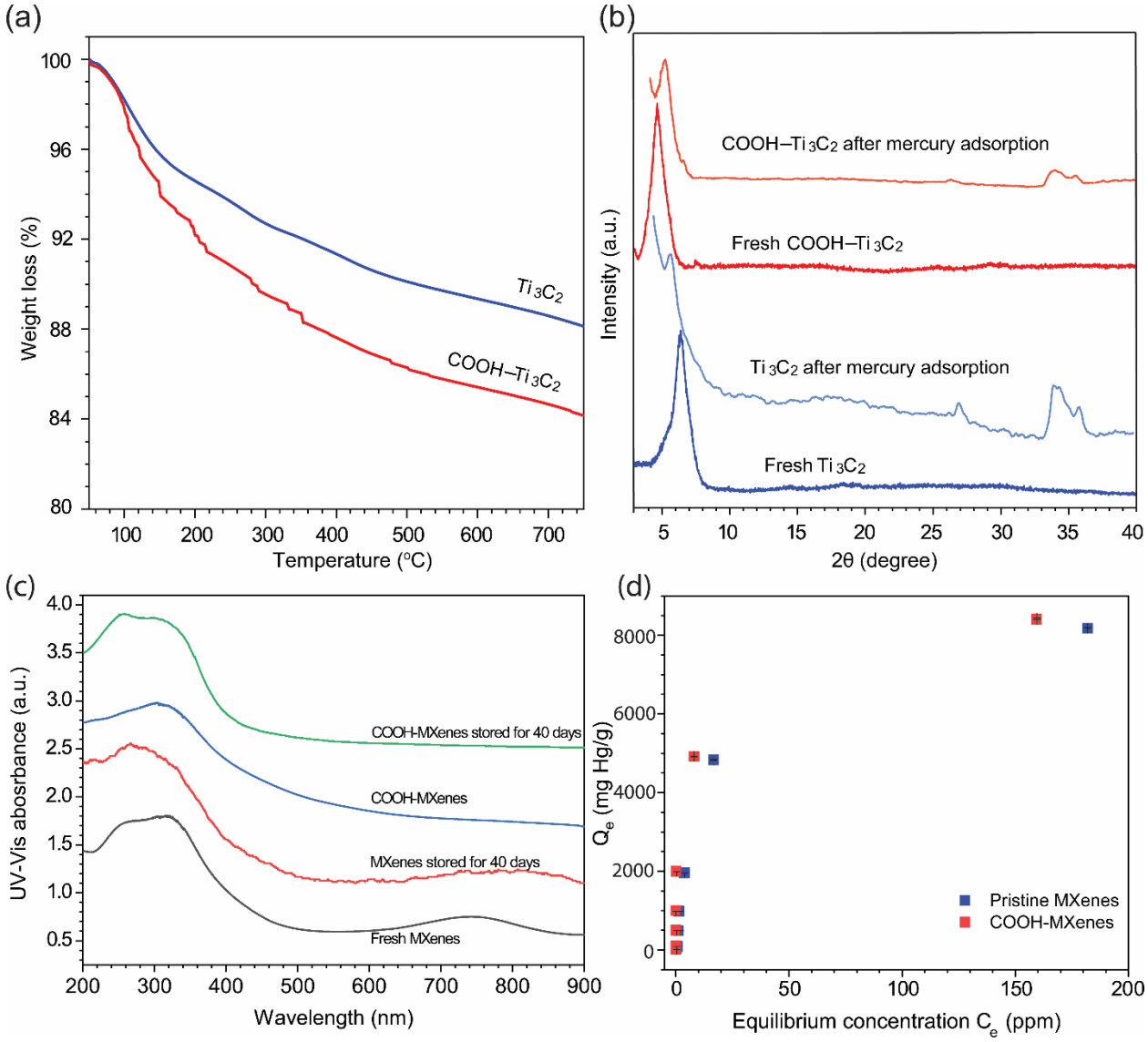

Figure 2. (a) TGA thermographs of $Ti_3C_2T_x$ and COOH–$Ti_3C_2T_x$ and (b) XRD patterns of $Ti_3C_2T_x$; COOH–$Ti_3C_2T_x$ before and after mercury adsorption with the initial concentration of 50 ppm. (c) UV-Vis spectra of the fresh and 40-day stored $Ti_3C_2T_x$ and COOH−$Ti_3C_2T_x$; (d) the equilibrium adsorption capacity of $Ti_3C_2T_x$ and COOH−$Ti_3C_2T_x$ at different Hg^{2+} concentrations (V/m=10 mL/mg).

[42], which disrupts the ordered MXene layers and reduces the intensity of the peak and interlayer spacing. Similar behavior had been observed for the adsorption of UO_2^{2+} by the 2D layered silicate RUB-15 [56]. Additionally, more adsorption of positively-charged mercury on the surface of functionalized MXene neutralizes the negative charge of MXenes and suppresses the repulsion forces between the layers [57].

The UV–Vis spectra of $Ti_3C_2T_x$ and COOH–$Ti_3C_2T_x$ (Figure 2c) show strong peaks between 280 to 330 nm [58-60]. In addition, the UV–Vis spectrum of $Ti_3C_2T_x$ has a distinct absorption peak at 770 nm. The disappearance of the peak at 770 nm is another proof that $Ti_3C_2T_x$ was carboxylated. The peak intensity at 770 nm was selected to assess the degradation of $Ti_3C_2T_x$, and the peak at 330 nm was considered for the degradation of COOH–$Ti_3C_2T_x$ [61, 62]. Both $Ti_3C_2T_x$ and COOH– $Ti_3C_2T_x$ colloidal solutions showed oxidation after 40 days. $Ti_3C_2T_x$ degraded faster than COOH–$Ti_3C_2T_x$, as the intensity of the peak at 330 nm decreased more for $Ti_3C_2T_x$. As deprotonation and the electrostatic repulsions between COOHs on the surface of COOH−$Ti_3C_2T_x$ are stronger than OHs on the surface of Ti_3C_2, the COOH−$Ti_3C_2T_x$ oxidizes slower than $Ti_3C_2T_x$ [63, 64].

3.2. Mercury Ions Adsorption

The mercury-ions adsorption capacities of $Ti_3C_2T_x$ and COOH−$Ti_3C_2T_x$ were examined at room temperature and a pH value of 6 using a batch method. 1 mg or 0.1 g $Ti_3C_2T_x$ and COOH–$Ti_3C_2T_x$ were added to 10 mL of a 1–1000 ppm Hg^{2+} aqueous solution, and the mixture was stirred for 24 h. As indicated in Table 1, the mercury-ion uptake and removal increase with an increased amount of the adsorbent. $Ti_3C_2T_x$ removed about 98.1% of mercury ions from a 200 ppm Hg^{2+} solution (V/m of 10 mL solution per 1 mg adsorbent), while COOH−$Ti_3C_2T_x$ removed 99.9%. This value is about half (~45.7%) when V/m was increased by 10 times (when 0.1 mg of $Ti_3C_2T_x$ in 10 mL

of solution was used). Expectedly, more active adsorption sites are accessible at higher adsorbent contents. However, the adsorption capacity is smaller at higher adsorbent dosages because of the smaller ratio of adsorbent to the pollutant. COOH–$Ti_3C_2T_x$ and $Ti_3C_2T_x$ demonstrated similarly high adsorption capacities (Figure 2d). However, COOH–$Ti_3C_2T_x$ has a significantly higher rate of adsorption. These indicate that the presence of carboxyl groups on the surface and the more negative surface charge of COOH–$Ti_3C_2T_x$ contribute more to the rate of adsorption, as is discussed later.

The effect of initial mercury-ion concentration on the capacity and the removal efficiency was investigated in the range of 1–1000 ppm (Figures 3a and 3b). The mercury uptake capacity increased with the initial Hg^{2+} concentration of both unmodified and modified $Ti_3C_2T_x$. This enhancement is explained by the stronger mass transfer driving force between the surface of adsorbents and the solute. However, the removal percentage slightly decreased at higher mercury contents. As seen in Figures 3a and 3b, this reduction is more severe in the mixtures with a lower amount of sorbents (i.e., V/m = 100 mL/mg). The mercury ions are likely are adsorbed on the

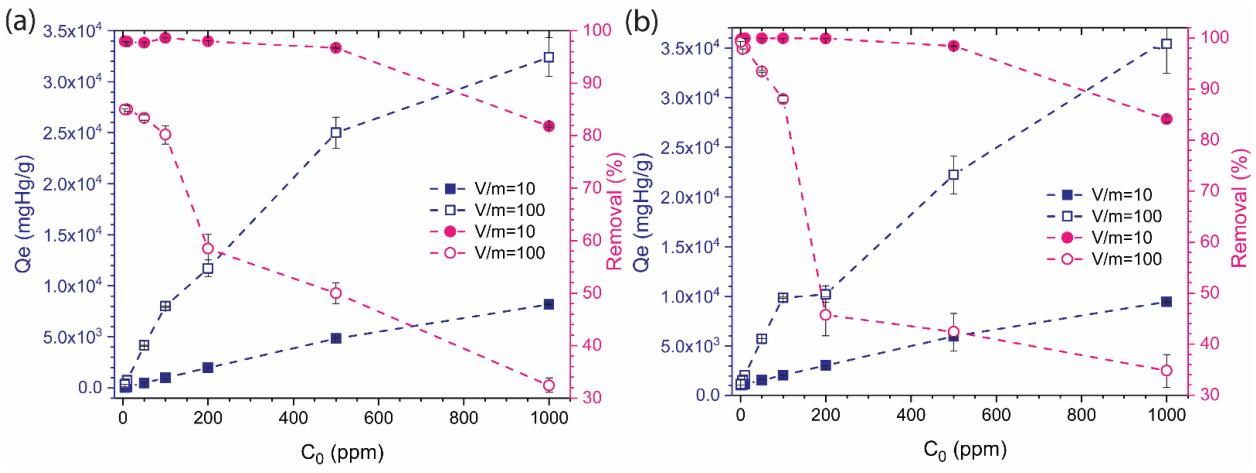

Figure 3. Equilibrium adsorption capacity and the removal percentage of mercury ions at two different ratios of the volume solution (mL) per adsorbent mass (mg) for (a) pristine $Ti_3C_2T_x$ and (b) COOH–$Ti_3C_2T_x$.

Table 1. The mercury adsorption parameters of $Ti_3C_2T_x$ and COOH–$Ti_3C_2T_x$ at different Hg^{2+} concentrations and two adsorbent dosages.

C_0	Pristine MXenes								COOH-functionalized MXenes							
	V/m=10 mL/mg				V/m= 100 mL/mg				V/m=10 mL/mg				V/m= 100 mL/mg			
	C_e	Q_e	R (%)	K_d	C_e	Q_e	R (%)	K_d	C_e	Q_e	R (%)	K_d	C_e	Q_e	R (%)	K_d
1000	182.00 ±5.20	8180.0 ±50.0	81.8 ±0.5	4.5e4 ±1.65e3	676.00 ±19.40	32400.0 ±1940.0	32.4 ±1.9	4.8e4 ±4.1e3	159.30 ±9.61	8407.0 ±92.1	84.1 ±0.9	5.3e4 ±3.7e3	652.00 ±32.40	34800.0 ±3200.0	34.8 ±3.2	5.3e4 ±0.7e4
500	16.70 ±1.10	4833.0 ±11.0	96.7 ±0.2	2.9e5 ±1.98e4	250.20 ±11.80	25000.0 ±1200	50.0 ±2.3	1.0e5 ±0.9e4	8.10 ±0.35	4919.0 ±3.7	98.4 ±0.1	6.1e5 ±2.0e4	288.00 ±20.50	21200.0 ±2050.0	42.4 ±4.1	7.4e4 ±1.2e4
200	3.81 ±0.10	1961.9 ±0.1	98.1 ±0.0	5.1e5 ±6.70e4	83.00 ±5.90	11700.0 ±590	58.5 ±2.9	1.4e5 ±1.5e4	0.11 ±0.10	1998.9 ±0.1	99.9 ±0.0	1.8e7 ±1.3e6	108.60 ±8.10	9140.0 ±810.0	45.7 ±4.1	8.4e4 ±1.3e4
100	1.36 ±0.12	986.4 ±5.4	98.6 ±0.1	7.2e5 ±6.21e4	19.80 ±2.10	8020.0 ±210	80.2 ±2.1	4.0e5 ±4.3e4	0.09 ±0.00	999.1 ±0.0	99.9 ±0.0	1.1e7 ±0.0	12.00 ±1.40	8800.0 ±140	88.0 ±1.4	7.3e5 ±8.4e4
50	1.16 ±0.10	488.4 ±0.1	97.7 ±0.0	4.2e5 ±3.71e3	8.30 ±0.61	4170.0 ±61	83.4 ±1.2	5.0e5 ±4.9e4	0.03 ±0.00	499.7 ±0.0	99.9 ±0.0	1.7e7 ±0.0	3.30 0.15	4670.0 ±15.0	93.4 ±0.3	1.4e6 ±5.0e4
10	0.31 ±0.01	97.0 ±0.1	97.0 ±0.0	3.2e5 ±1.04e4	1.6 ±0.10	840.0 ±9.9	84.0 ±1.1	5.2e5 ±4.6e4	0.01 ±0.00	99.9 ±0.0	99.9 ±0.0	1.4e7 ±0.0	0.20 ±0.00	980.0 ±0.0	98.0 ±0.0	4.9e6 ±0.0
5	0.16 ±0.0	48.4 ±0.0	96.8 ± n/a	3.1e5 ±0.0	0.81 ±0.00	420.0 ±0.0	84.0 ±0.0	5.2e5 ±0.0	0.00 ±0.00	49.9 ±0.0	99.9 ±0.0	1.0e7 ±0.0	0.11 ±0.00	489.0 ±0.0	98.0 ±0.0	4.4e6 ±0.0
1	0.02 ±0.0	9.8 ±0.0	98.0 ± 0.0	4.9e5 ± 0.0	0.14 ±0.00	86.0 ±0.0	86.0 ±0.0	6.1e5 ±0.0	0.00 ±0.00	10.0 ±0.0	99.9 ±0.0	3.3e6 ±0.0	0.01 ±0.00	99.2 ±0.0	99.2 ±0.0	1.2e7 ±0.0

C_0=initial concentration (ppm); C_e = equilibrium concentration (ppm); Q_e = equilibrium adsorption capacity (mg/g), R%= Hg removal; K_d= distribution coefficient (mL/g)

surface of MXenes sheets while the number of active sites is less at a lower adsorbent concentration.

The mercury-ion adsorption of $Ti_3C_2T_x$ and COOH–$Ti_3C_2T_x$ in 50 ppm and 200 ppm Hg^{2+} aqueous solutions (V/m=10 mL/mg) was evaluated for the different duration times within 0–180 min. More than 98% mercury-ion uptake from the 50-ppm solution in 5 min (Figures 4a and 4b) indicates that both $Ti_3C_2T_x$ and COOH–$Ti_3C_2T_x$ are effective adsorbents to remove mercury ions from wastewater due to their special structural properties and high density of surface functional groups. Generally, the adsorption mechanism of metal ions follows two steps; at first, the ions are quickly adsorbed on the available active sites, and the process is swift. The adsorption proceeds slower as the adsorption sites fill up, and the ions are required to diffuse into the pores and interlayer. The larger d-spacing of MXenes compared to other 2D materials such as GO, MoS_2, facilitates the second step. As observed in Figures 4c and 4d, $Ti_3C_2T_x$ demonstrates about 70% Hg^{2+} removal after 20 min. However, COOH–$Ti_3C_2T_x$ removed the same amount of mercury in

just 1 min at the same initial concentration (200 ppm), and the mercury-ion concentration dropped to less than 1 ppm in 10 min. The faster adsorption of COOH–$Ti_3C_2T_x$ can be related to the stronger binding of mercury ions to carboxylic moieties and more negative surface energy of COOH–$Ti_3C_2T_x$, which increases the electrostatic interactions of COOH–$Ti_3C_2T_x$. Figure 4e shows the adsorption kinetics results of $Ti_3C_2T_x$ and COOH–$Ti_3C_2T_x$. The removal rate of Hg^{2+} increased quickly and then leveled off at 10 and 60 min for COOH–$Ti_3C_2T_x$ and $Ti_3C_2T_x$, respectively. This rapid mercury removal at the beginning of the process can be explained by high initial concentration of Hg^{2+} and thereby a larger driving force, while the saturation of adsorbent sites

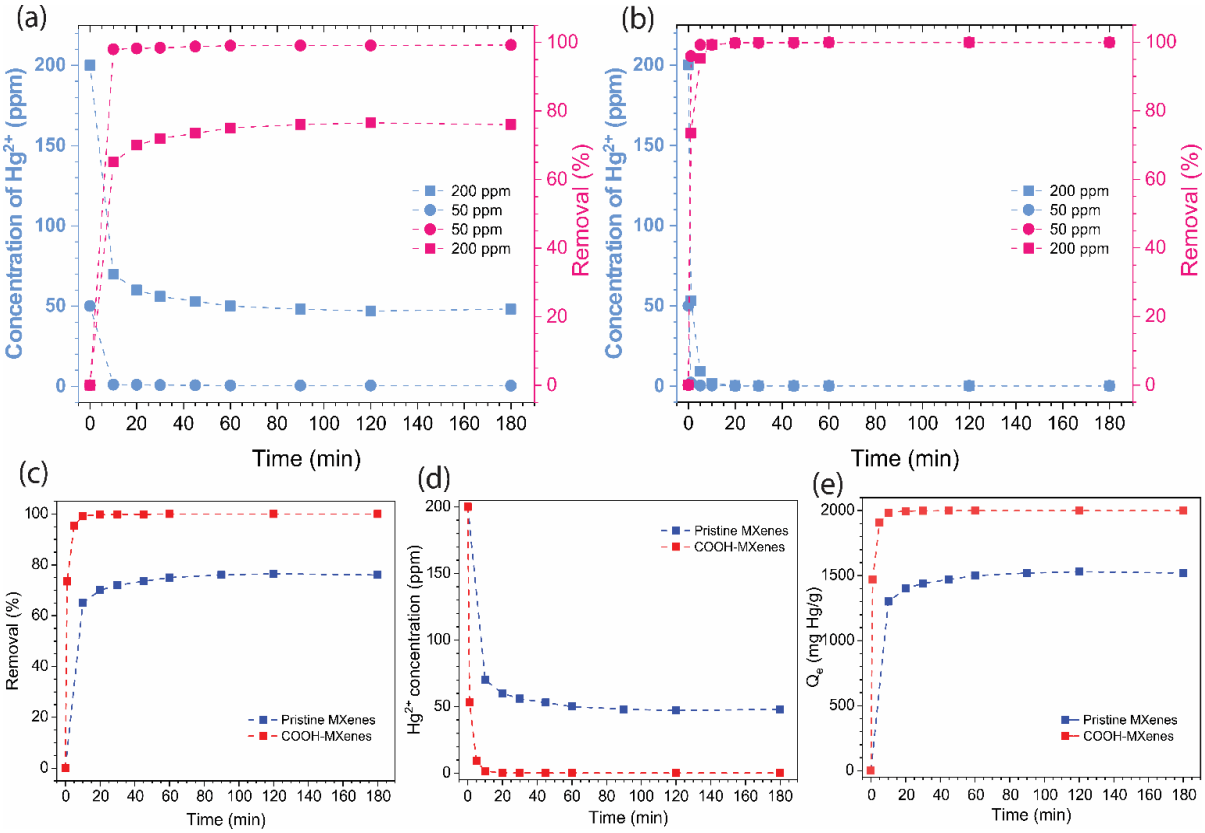

Figure 4. Adsorption-time study: The concentration and the removal percentage of mercury from a 200 ppm and 50 ppm solution ($\frac{V}{m} = 10\ mL/mg$) for (a) $Ti_3C_2T_x$ and (b) COOH–$Ti_3C_2T_x$; (c) the mercury removal; and (d) the Hg^{2+} concentration and (e) the equilibrium adsorption of $Ti_3C_2T_x$ and COOH–$Ti_3C_2T_x$ from a 200 ppm solution ($\frac{V}{m} = 10\ mL/mg$) *vs.* time.

results in a slower adsorption rate. The results indicate that COOH–$Ti_3C_2T_x$ is a more efficient sorbent than $Ti_3C_2T_x$ for mercury-ion removal.

Morphological characteristics of COOH–$Ti_3C_2T_x$ before and after the adsorption were evaluated by SEM (Figure S2a and S2b). The surface of COOH–$Ti_3C_2T_x$–Hg is more rough after mercury ions are settled on, and the SEM-EDX is evidence for the mercury-ion adsorption on the surface of COOH–$Ti_3C_2T_x$. Additionally, the UV and FTIR spectra of the MXenes revealed some changes before and after the adsorption test (Figures S2c and S2d) due to interactions between the mercury ions and the functional groups on the surface. The appearance of new bands at 1300 cm^{-1} and 1700 cm^{-1} can be related to the interactions between mercury and the functional groups (COOH, OH) on the surface of the adsorbent. Similar results have been reported for mercury-ion adsorption by other sorbents [65].

The distribution coefficient (K_d) is an important parameter for assessing the performance and affinity of the sorbents on a target metal ion. The K_d is defined as [66, 67]:

$$K_d = \frac{(C_0 - C_e)}{C_e}\frac{V}{m} \quad (5)$$

Where C_0 ($mg \cdot L^{-1}$) is the initial metal ion concentration, C_e ($mg \cdot L^{-1}$) is the equilibrium metal ion concentration (the amount of unabsorbed mercury), V (mL) is the volume of the aqueous media, and m is the mass (g) of adsorbent.

The K_d reflects the affinity of the adsorbents to the heavy metals, and values greater than 1.0×10^5 $mL \cdot g^{-1}$ represent suitable sorbents [68]. The K_d values of $Ti_3C_2T_x$ and COOH–$Ti_3C_2T_x$ for Hg^{2+} adsorption are 4.2×10^5 and 1.7×10^7 $mL \cdot g^{-1}$, respectively, which are among the highest values for mercury-ion adsorption (Table 1), indicating that Hg^{2+} binds effectively to $Ti_3C_2T_x$ surface. Figure 5 compares mercury-ion adsorption K_d values of COOH–$Ti_3C_2T_x$ and $Ti_3C_2T_x$ with

346 those of well-known benchmark adsorbents; the Hg^{2+} distribution coefficient of COOH–$Ti_3C_2T_x$

347 is among the highest reported values in the literature.

348 **3.2.1 Effect of pH on Adsorption Capacity**

349 $Ti_3C_2T_x$ and COOH–$Ti_3C_2T_x$ demonstrated high mercury uptake in the pH range of 2-6 (Figure

350 6a). pH of the effluent is important as the ion complexes, surface charge, and functionalities of the

351 adsorbent can change with pH. The adsorption capacity of COOH–$Ti_3C_2T_x$ increased slightly

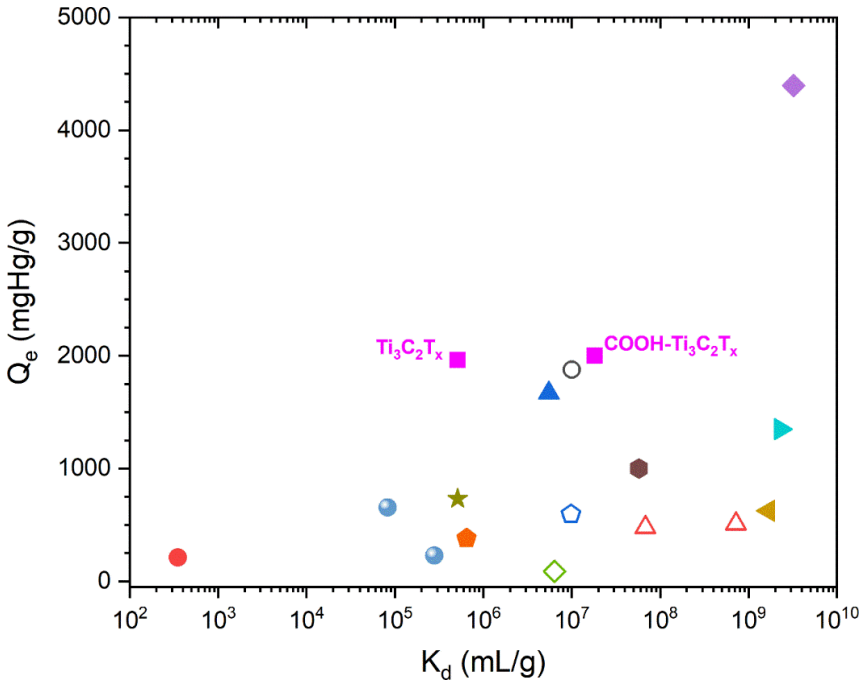

352 Figure 5. Comparison the distribution coefficient and the equilibrium adsorption capacity of

353 $Ti_3C_2T_x$ and COOH–$Ti_3C_2T_x$ with other adsorbent in the literature: red filled circle (Fe-BTC) and

354 blue filled triangle (Fe-BTC/PDA) [69], purple filled diamond (TPB-DMTP-COFSH) [70], orange

355 filled left-pointing triangle (NanoSe Sponge) [71], green filled right-pointing triangle (COF-S-SH)

356 [72], brown hexagonal (PAF-1-SH) [73], light brown star (S-FMC-900) [68], red pentagon

357 (LMOF-263) [74], light blue filled circles (DMS-Fe3O4) [75], open diamond (LHMS-1) [76],

358 black open circle (SCTN-1) [77], red-open triangles (Chalcogenide glass) [78], blue open pentagon

359 (Mn-MoS4) [79].

360

with an increase in pH in the range of 2–3, while that of $Ti_3C_2T_x$ remained almost constant. Earlier, we discussed less the negative surface charge of $Ti_3C_2T_x$ and COOH–$Ti_3C_2T_x$ at lower pH values, which can adversely affect their efficacy for adsorption of the positively-charged Hg ions. On the other hand, Hg^{2+} is the dominant ion in acidic solutions, while it is hydrolyzed to $Hg(OH)^+$ by moving to neutral pH values [80]. It seems that the more positively-charged mercury ions at lower pH compensate for the opposite effect of the less negatively charged surface of MXenes. In addition, it has been reported that mercury ions tend to form covalent bonds, which are less impacted by pH values than ionic interactions [81].

3.2.2. Mercury Leaching

The potential leaching of adsorbed mercury on $Ti_3C_2T_x$ and COOH–$Ti_3C_2T_x$ was determined at two initial Hg concentrations. After seven days of stirring at room temperature, the maximum mercury-ion concentration is 30 µg/L for $Ti_3C_2T_x$ (Figure 6b). This amount is within the safe limit recommended by EPA (<200µg/L) to classify it as an industrial hazardous waste [82]. The amount of mercury leachate from COOH–$Ti_3C_2T_x$ is much lower than that from $Ti_3C_2T_x$ due to the strong

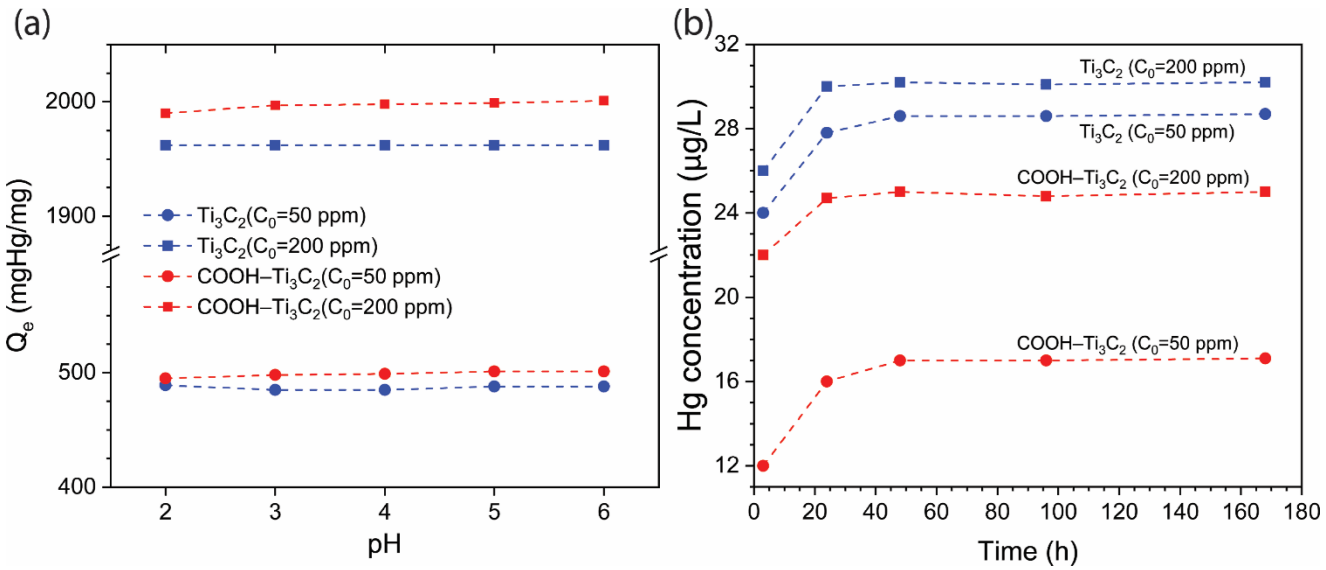

Figure 6. (a) Mercury uptake of $Ti_3C_2T_x$ and COOH–$Ti_3C_2T_x$ at different pH values; (b) the mercury leaching from the adsorbents *vs.* the extraction time.

interactions between mercury ions and the COOH functional groups. The mercury content in leachate for both samples increased with increased initial concentration, but for both samples, it is still much lower than the safe limit defined by the US EPA. The leaching rate of mercury ions into the solution was fast at the beginning of the extraction process, while it gradually slowed down by the extraction time. As a large amount of soluble mercury ions was leached out to the solution during 24 h, the concentration gradient inside the adsorbents layers and leachate decreased, resulting in a slower extraction rate. Moreover, the covalently-bonded mercury on $Ti_3C_2T_x$ and COOH–$Ti_3C_2T_x$ is unable to leach out into the solution.

3.2.3. Kinetics of Adsorption

Figure 4e indicated that the mercury-ion adsorption is very fast initially and the rate of the adsorption decreases with time quickly. COOH–$Ti_3C_2T_x$ reaches the equilibrium state much earlier than $Ti_3C_2T_x$ due to its more negativity of the surface and stronger interactions. We investigated the kinetics of the adsorption process via fitting the data to the Lagergren pseudo-first order and the Ho's pseudo-second order models (Figure 7). These models respectively are [83, 84]:

$$\text{Log } (Q_t - Q_e) = \log Q_e - \frac{k_1 t}{2.303} \quad (6)$$

$$\frac{t}{Q_t} = \frac{1}{k_2 Q_e^2} + \frac{t}{Q_e} \quad (7)$$

where k_1 (min^{-1}) and k_2 ($\text{g} \cdot \text{m} g^{-1} min^{-1}$) are the pseudo-first order and the pseudo-second order rate constants, respectively. Q_e and Q_t are the mercury-ion adsorption capacity ($\text{mg} \cdot \text{g}^{-1}$) at equilibrium and t (adsorption time, min), respectively.

The estimated model parameters are given in Table S1. Figure 7a indicates that the plot of ln (Q_e– Q_t) versus time is not linear, and the calculated Q_e is not close to the experimental data; in contrast, the Q_e obtained from the pseudo-second-order kinetic model is 1600 mg/g and 2000 mg/g for $Ti_3C_2T_x$ and COOH–$Ti_3C_2T_x$, respectively, are close to the experimental values (Figure 7b).

Furthermore, the pseudo-second-order kinetic model has the highest R^2 values (almost 1). This result indicates that the pseudo-second-order kinetic model is more representative of the experimental data, and the mercury-ion adsorption on $Ti_3C_2T_x$ and COOH–$Ti_3C_2T_x$ is governed by a chemical adsorption process [72, 85]. In addition, we investigated the initial adsorption behavior (h_i) of the metal ions on $Ti_3C_2T_x$ and COOH–$Ti_3C_2T_x$ via comparison of the sorbent h_1 ($h_1 = k_1 Q_e$) and h_2 values ($h_2 = k_2 Q_e^2$) (mg/g.min). Table S1 indicates that the initial adsorption rates of COOH–$Ti_3C_2T_x$ were higher than $Ti_3C_2T_x$ in both models. The high h_2 value of COOH–$Ti_3C_2T_x$ points to more capability of COOHs groups compared to the OHs ones to bind with Hg^{2+}. The results confirm that the COOHs on the surface of COOH–$Ti_3C_2T_x$ affected not only the initial adsorption rate but also contributed to the increase of the mercury-ion diffusion between the COOH–$Ti_3C_2T_x$ layers by increasing the interlayer distance.

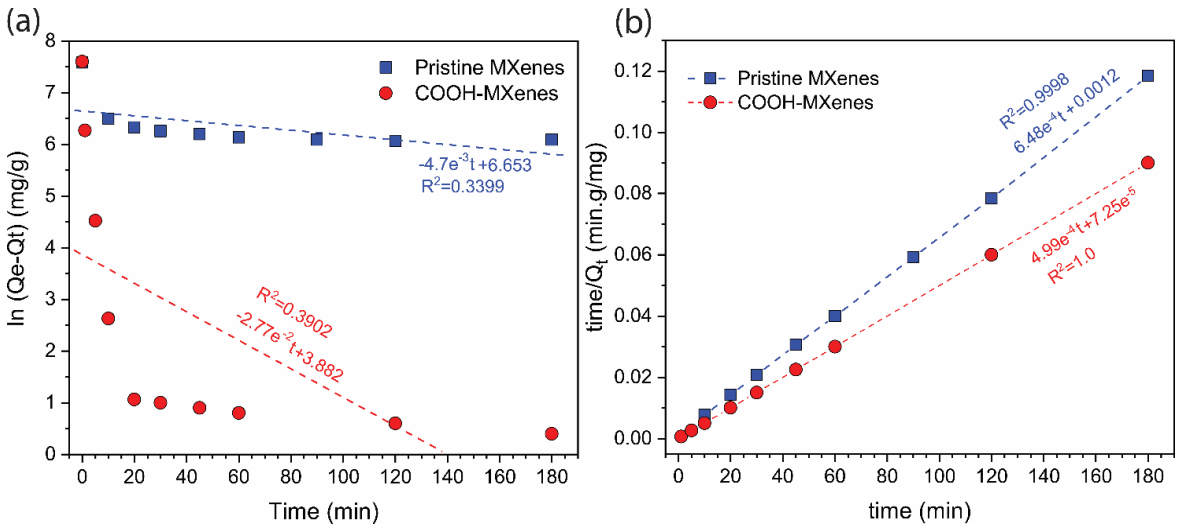

Figure 7. (a) Pseudo-first-order and (b) pseudo-second-order of the mercury adsorption on $Ti_3C_2T_x$ and COOH–$Ti_3C_2T_x$ (C_0 = 200 ppm, $\frac{V}{m} = 10\ mL/mg$).

3.2.2. Equilibrium Isotherms

Langmuir and Freundlich isotherm models were used to calculate the equilibrium constants and mercury-ion adsorption capacities of COOH–$Ti_3C_2T_x$ and $Ti_3C_2T_x$ (Figure S3) [67, 85].

Langmuir model: $$\frac{C_e}{Q_e} = \frac{C_e}{Q_{max}} + \frac{K_L}{Q_{max}} \quad (8)$$

Freundlich model: $$\ln Q_e = \ln K_F + n \ln C_e \quad (9)$$

where C_e (L/g) is the equilibrium concentration, K_L (L/g) is the Langmuir adsorption constant, Q_{max} is the theoretical maximum capacity, and K_F (mg/g)(L/mg)$^{1/n}$ and n are the Freundlich constants. Figure S3 shows how the two models fit the experimental data, and Table 2 gives the model parameter estimates. The Langmuir isotherms model represents the data better [have higher R^2 values (~0.99)] than the Freundlich model, indicating that the mercury adsorption on the $Ti_3C_2T_x$ and COOH–$Ti_3C_2T_x$ are more likely monolayer adsorption [86-88].

3.2.3. Adsorption Mechanism

Understanding the adsorption mechanism of mercury ions onto COOH–$Ti_3C_2T_x$ surface is essential to comprehend the effects of surface functionality on the efficiency of the process. Surface physicochemical properties such as the surface area, terminal groups, hydrophilicity, and surface charge can influence the interactions between MIs and $Ti_3C_2T_x$–COOH. The results

Table 2. Parameter values obtained from fitting Langmuir model and Freundlich models to the $Ti_3C_2T_x$ and COOH–$Ti_3C_2T_x$ adsorption data.

Adsorbent	Langmuir adsorption model			Freundlich adsorption model		
	K_L (L/g)	Q_{max} (mg.g^{-1})	R^2	K_F ((mg/g)(L/mg)$^{1/n}$)	n	R^2
Ti_3C_2	22.0	10^4	0.9893	338.66	0.80	0.9275
COOH–Ti_3C_2	2.0	10^4	0.9989	1461.91	0.54	0.7818

revealed that different mercury adsorption mechanisms, electrostatic interaction [6, 26, 89], surface complexation [88, 90], and mercury (II) reduction [91] are likely to be involved in this study.

Electrostatic attractions. Mercury ions can be adsorbed on COOH–$Ti_3C_2T_x$ via electrostatic attractions between their positive charges and the negatively charged surface of the hydrophilic nanosheets (Figure 8) [88]. The electrostatic attraction can be detected by the adsorption behavior at different pH values, where the mercury removal was almost unchanged due to the electrostatic interaction of MXene surface functional groups with Hg^{2+} and $Hg(OH)^{+}$ at low and high pH values. In addition, better adsorption of more negatively-charged COOH–$Ti_3C_2T_x$ compared to the less-negatively charged pristine $Ti_3C_2T_x$ suggested the electrostatic interaction

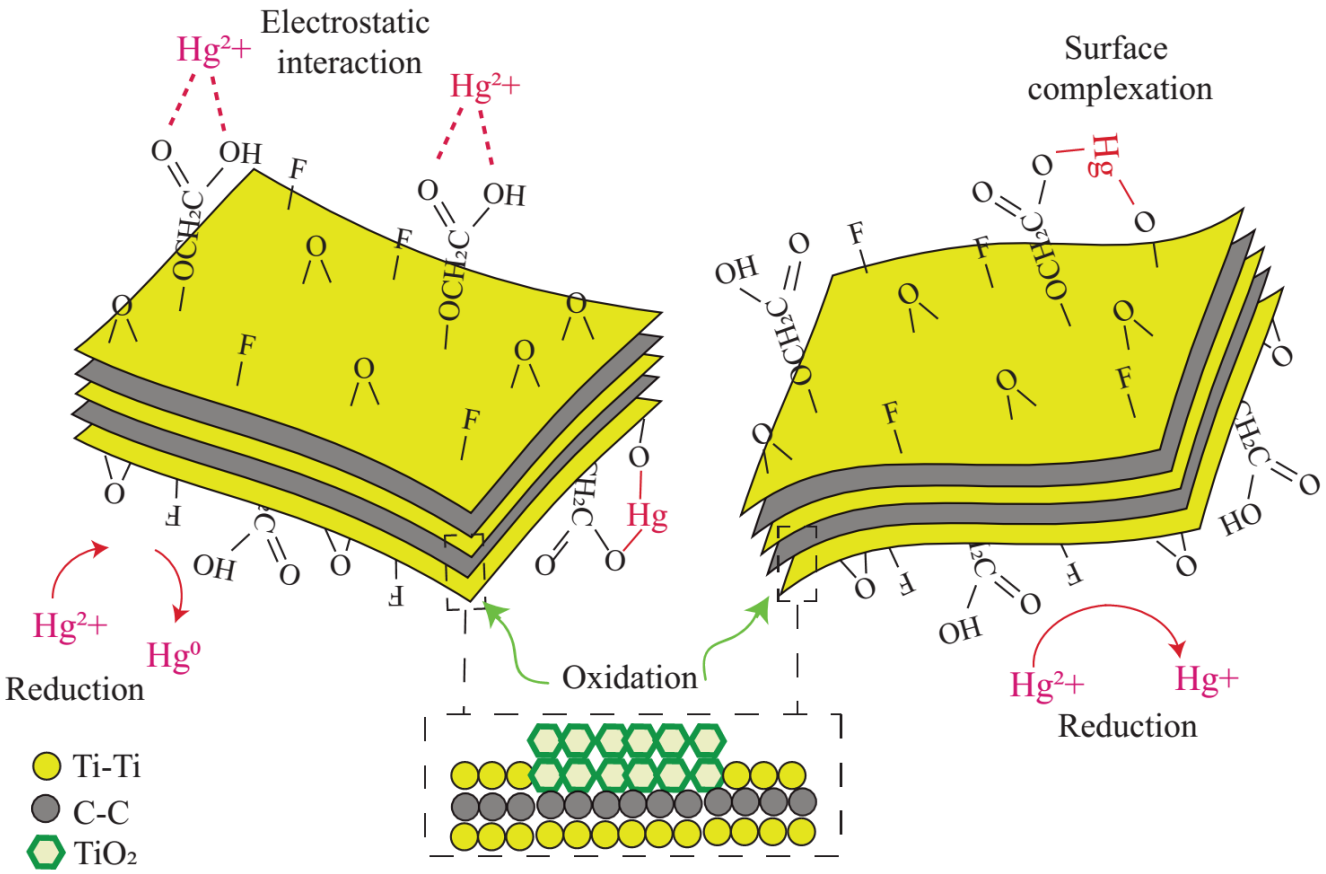

Figure 8. Schematic representation of the adsorption mechanisms of mercury ions to COOH–$Ti_3C_2T_x$.

mechanism for this system. The high density of functional groups on the surface of COOH–$Ti_3C_2T_x$ can facilitate mercury-ion removal via electrostatic interactions between Ti–O and Ti–COOH and Hg^{2+} [40]. Needless to say, cations are always adsorbed by negatively-charged sorbents, and hydrophilicity has a positive effect on the adsorption. More negative surface charge of COOH–$Ti_3C_2T_x$ than $Ti_3C_2T_x$ and lower hydration energy of Hg^{2+} compared to Cu^{2+} [92] signifies the importance of this mechanism for adsorption of MIs on COOH–$Ti_3C_2T_x$.

Surface complexation. The presence of carboxyl groups enhances affinity between Ti–COOH and Hg^{2+} ions, which may lead to inner-sphere complex formation onto the surface of COOH–$Ti_3C_2T_x$ [22, 23, 88, 93], as shown in Figure 8. The appearance of the peak at 500 cm^{-1} confirms the existence of complexation between Hg ions and the functional groups (Ti-O-Hg) (Figure S2d). The interaction of Hg with the functional groups of $Ti_3C_2T_x$ has also been confirmed via FTIR and XPS spectroscopy elsewhere [36]. Compared to $Ti_3C_2T_x$, COOH–$Ti_3C_2T_x$ has a higher tendency to contribute to the surface complexation because of its carboxyl groups [94]. It has also been reported that carboxyl groups tend to interact with heavy metal ions, and participate in the chemisorption mechanism more than hydroxyl groups [42]. This also explains the higher mercury-ion adsorption of COOH–$Ti_3C_2T_x$.

Reduction-oxidation. The faster mercury adsorption of COOH–$Ti_3C_2T_x$ suggests that the ion removal should be via more than a simple electrostatic interaction mechanism. Reductive adsorption of heavy metals ions (e.g. Hg (II), Cr (VI), Cu (II), Fe (III)) on a MXene has been reported by others [38]. As shown in Figure 8, the reduction-oxidation mechanism leads to the reduction of Hg^{2+} to Hg^{+} and Hg^{0}, and also to the formation of white TiO_2 particles, as confirmed by XRD peak at $2\theta = 35^{o}$, and XPS elsewhere [95]. The white precipitation during the adsorption test has also been reported elsewhere [26]. Wang et al. reported that the surface redox reaction

460 involves a partial electron transfer from Ti atoms on the surface of $Ti_3C_2T_x$ flakes [96]. This
461 irreversible oxidation process can deteriorate the adsorption capacity of MXene after a few
462 adsorption-desorption cycles, as will be discussed later.

463 **3.3. Adsorbent Regeneration**

464 Regeneration is one of the important steps of the adsorption process which can decrease the process
465 cost significantly and protect the environment [3, 97, 98], as the regenerated sorbents can be used
466 again in the process. After attaining the adsorption equilibrium, our absorbents, COOH–$Ti_3C_2T_x$
467 and $Ti_3C_2T_x$, were collected and washed with 10% W/V thiourea in 0.1 M HCl, followed by 1M
468 HNO_3 to recover the adsorbents. The mercury removal efficiencies of COOH–$Ti_3C_2T_x$ and $Ti_3C_2T_x$
469 decreased from 99.9% to 95.3% and 83.4%, respectively, after 3 cycles (Figure 9). The reduction
470 in mercury uptake is explained by the partial oxidation of MXenes into TiO_2, and the possible
471 chemical bonds between the adsorbents and ions (i.e., incomplete desorption of metal ions from
472 the surface). The regeneration study also confirmed the higher stability of the functionalized
473 MXenes against oxidation in an aqueous solution, which agrees with our XRD data.

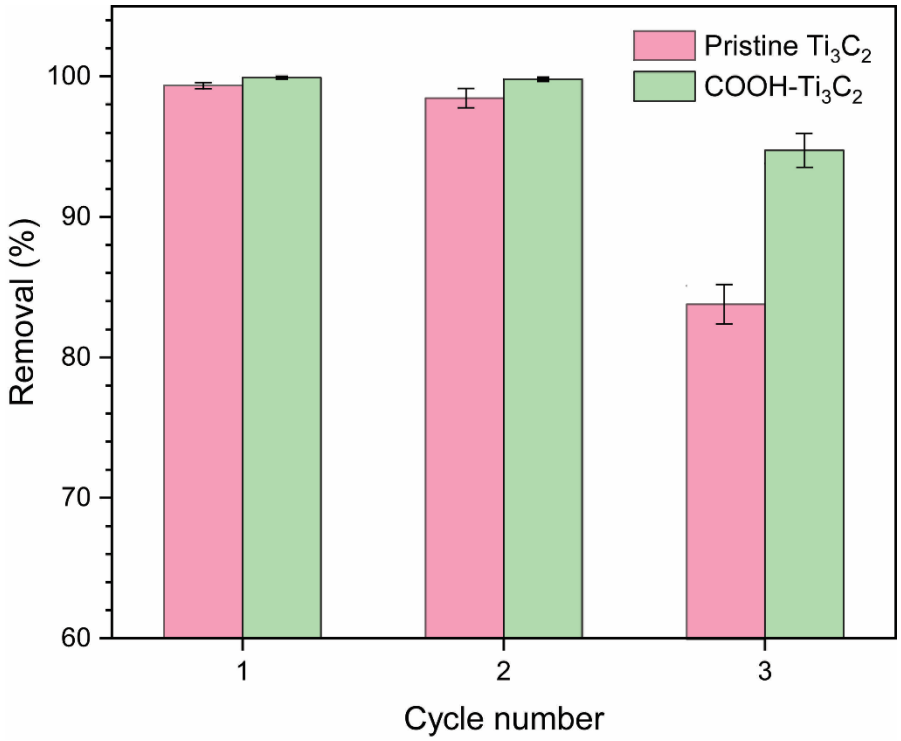

Figure 9. The mercury removal (%) efficiency of COOH−$Ti_3C_2T_x$ and $Ti_3C_2T_x$ at different number of adsorption–desorption cycles from 50 ppm aqueous solution.

4. Conclusions

This work presented a simple one-step method of $Ti_3C_2T_x$ carboxylation that involves the use of a chelating agent with a linear structure, providing strong carboxylic acid groups with high mobility. It investigated how introducing carboxyl functional groups on the surface of $Ti_3C_2T_x$ MXene affects the ability of $Ti_3C_2T_x$ to adsorb mercury. The carboxylation of $Ti_3C_2T_x$ at room temperature resulted in fast and efficient adsorption of mercury ions from water. The surface of the functionalized $Ti_3C_2T_x$ (COOH–$Ti_3C_2T_x$) exhibited a more negative surface charge over a pH range of 2.0 to 8.5. In addition, surface modification increased the interlayer spacing of $Ti_3C_2T_x$ nanosheets and their oxidation stability. The stability and the rate of mercury ions adsorption was also improved compared to the pristine $Ti_3C_2T_x$ in the pH range values of 2–6. The adsorption

capacity and distribution coefficient of COOH–$Ti_3C_2T_x$ in a 50 ppm Hg^{2+} solution (pH=6) significantly increased to 499.7 mg/g and 1.67×10^7 mL/g from 488.4 mg/g and 4.2×10^5 mL/g for the pristine $Ti_3C_2T_x$. The adsorption capacity increased gradually by increasing the Hg^{2+} concentration in water while the removal efficiently slightly decreased. The removal percentage was also decreased significantly at lower adsorbents dosage because of the limitation of adsorptive sites. COOH–$Ti_3C_2T_x$ exhibited significantly faster mercury-ion uptake compared to the pristine $Ti_3C_2T_x$, and the adsorption reaches the equilibrium condition in less than 10 min. The mercury uptake by COOH functionalized MXenes were more stable than the pristine MXenes during a seven-day leaching test experiment. Also, the mercury concentration in the extract solution (16μg/L) is about 10% of the defined safety limit by the EPA organization. The K_d value of COOH–$Ti_3C_2T_x$ for Hg^{2+} removal is 1.7×10^7 $mL\cdot g^{-1}$, which is among the highest values for mercury-ion adsorption reported in the literature. The chemisorption and electrostatic interactions between the carboxyl groups and Hg^{2+} are responsible for high adsorption performance of COOH–$Ti_3C_2T_x$. The Langmuir isotherm and the pseudo-second order kinetic models predicted that the adsorption of mercury ions was taken place between nanosheets interlayer and the COOH moieties accelerated the ions diffusivity between the sheets, resulting in fast and efficient mercury-ion removal from aqueous effluents. COOH–$Ti_3C_2T_x$ has industrial potential for efficient removal of heavy metal ions, as it has a higher mercury-ion uptake capacity than commercially available adsorbents reported in the literature.

Acknowledgment

Ahmad A. Shamsabadi and Ali Pournaghshband Isfahani were partially supported by the U.S. National Science Foundation under Grant No. CBET–1804285. Any opinions, findings, and conclusions or recommendations expressed in this material are those of the authors and do not

necessarily reflect the views of the National Science Foundation. The authors would like to thank Babak Anasori, Yury Gogotsi, Vibha Kalra, Daniel R. Strongin, and Steven Wrenn for their invaluable support.

References

[1] J. Yang, W. Zhu, W. Qu, Z. Yang, J. Wang, M. Zhang, H. Li, Selenium Functionalized Metal–Organic Framework MIL-101 for Efficient and Permanent Sequestration of Mercury, Environmental science & technology, 53 (2019) 2260-2268.

[2] M. Naushad, T. Ahamad, Z.A. AlOthman, H. Ala'a, Green and eco-friendly nanocomposite for the removal of toxic Hg (II) metal ion from aqueous environment: adsorption kinetics & isotherm modelling, Journal of Molecular Liquids, 279 (2019) 1-8.

[3] D. An, X. Wang, X. Cheng, L. Cui, X. Zhang, P. Zhou, Y. Dong, Regeneration performance of activated coke for elemental mercury removal by microwave and thermal methods, Fuel Processing Technology, 199 (2020) 106303.

[4] P.T. Bolger, D.C. Szlag, An electrochemical system for removing and recovering elemental mercury from a gas stream, Environmental science & technology, 36 (2002) 4430-4435.

[5] M. Naushad, T. Ahamad, B.M. Al-Maswari, A.A. Alqadami, S.M. Alshehri, Nickel ferrite bearing nitrogen-doped mesoporous carbon as efficient adsorbent for the removal of highly toxic metal ion from aqueous medium, Chemical Engineering Journal, 330 (2017) 1351-1360.

[6] A. Shahzad, K. Rasool, W. Miran, M. Nawaz, J. Jang, K.A. Mahmoud, D.S. Lee, Mercuric ion capturing by recoverable titanium carbide magnetic nanocomposite, Journal of hazardous materials, 344 (2018) 811-818.

[7] K. Leus, K. Folens, N.R. Nicomel, J.P.H. Perez, M. Filippousi, M. Meledina, M.M. Dîrtu, S. Turner, G. Van Tendeloo, Y. Garcia, Removal of arsenic and mercury species from water by covalent triazine framework encapsulated γ-Fe2O3 nanoparticles, Journal of hazardous materials, 353 (2018) 312-319.

[8] S. Wang, E. Ariyanto, Competitive adsorption of malachite green and Pb ions on natural zeolite, Journal of Colloid and Interface Science, 314 (2007) 25-31.

[9] D. Yang, Z. Zheng, H. Liu, H. Zhu, X. Ke, Y. Xu, D. Wu, Y. Sun, Layered titanate nanofibers as efficient adsorbents for removal of toxic radioactive and heavy metal ions from water, The Journal of Physical Chemistry C, 112 (2008) 16275-16280.

[10] S. Yu, H. Pang, S. Huang, H. Tang, S. Wang, M. Qiu, Z. Chen, H. Yang, G. Song, D. Fu, Recent advances in metal-organic framework membranes for water treatment: A review, Science of The Total Environment, 800 (2021) 149662.

[11] P.N. Diagboya, B.I. Olu-Owolabi, K.O. Adebowale, Synthesis of covalently bonded graphene oxide–iron magnetic nanoparticles and the kinetics of mercury removal, Rsc Advances, 5 (2015) 2536-2542.

[12] L. Cui, Y. Wang, L. Gao, L. Hu, L. Yan, Q. Wei, B. Du, EDTA functionalized magnetic graphene oxide for removal of Pb (II), Hg (II) and Cu (II) in water treatment: Adsorption mechanism and separation property, Chemical engineering journal, 281 (2015) 1-10.

[13] E. Rathore, K. Biswas, Selective and ppb level removal of Hg (ii) from water: synergistic role of graphene oxide and SnS 2, Journal of Materials Chemistry A, 6 (2018) 13142-13152.

[14] L. Fu, Z. Yan, Q. Zhao, H. Yang, Novel 2D nanosheets with potential applications in heavy metal purification: A review, Advanced Materials Interfaces, 5 (2018) 1801094.

[15] M.C. Duch, G.S. Budinger, Y.T. Liang, S. Soberanes, D. Urich, S.E. Chiarella, L.A. Campochiaro, A. Gonzalez, N.S. Chandel, M.C. Hersam, Minimizing oxidation and stable nanoscale dispersion improves the biocompatibility of graphene in the lung, Nano letters, 11 (2011) 5201-5207.

[16] Z. Ding, Z. Zhang, H. Ma, Y. Chen, In vitro hemocompatibility and toxic mechanism of graphene oxide on human peripheral blood T lymphocytes and serum albumin, ACS applied materials & interfaces, 6 (2014) 19797-19807.

[17] Z. Wang, B. Mi, Environmental applications of 2D molybdenum disulfide (MoS2) nanosheets, Environmental science & technology, 51 (2017) 8229-8244.

[18] Z. Wang, A. Sim, J.J. Urban, B. Mi, Removal and recovery of heavy metal ions by two-dimensional MoS2 nanosheets: Performance and mechanisms, Environmental science & technology, 52 (2018) 9741-9748.

[19] K. Rasool, R.P. Pandey, P.A. Rasheed, S. Buczek, Y. Gogotsi, K.A. Mahmoud, Water treatment and environmental remediation applications of two-dimensional metal carbides (MXenes), Materials Today, (2019).
[20] S. Yu, H. Tang, D. Zhang, S. Wang, M. Qiu, G. Song, D. Fu, B. Hu, X. Wang, MXenes as emerging nanomaterials in water purification and environmental remediation, Science of The Total Environment, (2021) 152280.
[21] J. Guo, Q. Peng, H. Fu, G. Zou, Q. Zhang, Heavy-metal adsorption behavior of two-dimensional alkalization-intercalated MXene by first-principles calculations, The Journal of Physical Chemistry C, 119 (2015) 20923-20930.
[22] Q. Peng, J. Guo, Q. Zhang, J. Xiang, B. Liu, A. Zhou, R. Liu, Y. Tian, Unique lead adsorption behavior of activated hydroxyl group in two-dimensional titanium carbide, Journal of the American Chemical Society, 136 (2014) 4113-4116.
[23] A. Shahzad, K. Rasool, W. Miran, M. Nawaz, J. Jang, K.A. Mahmoud, D.S. Lee, Two-dimensional Ti3C2T x MXene nanosheets for efficient copper removal from water, ACS Sustainable Chemistry & Engineering, 5 (2017) 11481-11488.
[24] V. Chandra, J. Park, Y. Chun, J.W. Lee, I.-C. Hwang, K.S. Kim, Water-dispersible magnetite-reduced graphene oxide composites for arsenic removal, ACS nano, 4 (2010) 3979-3986.
[25] J.N. Tiwari, K. Mahesh, N.H. Le, K.C. Kemp, R. Timilsina, R.N. Tiwari, K.S. Kim, Reduced graphene oxide-based hydrogels for the efficient capture of dye pollutants from aqueous solutions, Carbon, 56 (2013) 173-182.
[26] Y. Ying, Y. Liu, X. Wang, Y. Mao, W. Cao, P. Hu, X. Peng, Two-dimensional titanium carbide for efficiently reductive removal of highly toxic chromium (VI) from water, ACS applied materials & interfaces, 7 (2015) 1795-1803.
[27] M. Naguib, V.N. Mochalin, M.W. Barsoum, Y. Gogotsi, 25th anniversary article: MXenes: a new family of two-dimensional materials, Advanced materials, 26 (2014) 992-1005.
[28] B. Anasori, Y. Xie, M. Beidaghi, J. Lu, B.C. Hosler, L. Hultman, P.R. Kent, Y. Gogotsi, M.W. Barsoum, Two-dimensional, ordered, double transition metals carbides (MXenes), ACS nano, 9 (2015) 9507-9516.
[29] O. Mashtalir, M.R. Lukatskaya, M.Q. Zhao, M.W. Barsoum, Y. Gogotsi, Amine-assisted delamination of Nb2C MXene for Li-Ion energy storage devices, Advanced Materials, 27 (2015) 3501-3506.
[30] K. Rasool, K.A. Mahmoud, D.J. Johnson, M. Helal, G.R. Berdiyorov, Y. Gogotsi, Efficient Antibacterial Membrane based on Two-Dimensional Ti 3 C 2 T x (MXene) Nanosheets, Scientific reports, 7 (2017) 1598.
[31] A. Arabi Shamsabadi, M. Sharifian Gh, B. Anasori, M. Soroush, Antimicrobial Mode-of-Action of Colloidal Ti3C2T x MXene Nanosheets, ACS Sustainable Chemistry & Engineering, 6 (2018) 16586-16596.
[32] I. Ihsanullah, MXenes (two-dimensional metal carbides) as emerging nanomaterials for water purification: Progress, challenges and prospects, Chemical Engineering Journal, 388 (2020) 124340.
[33] C.J. Zhang, S. Pinilla, N. McEvoy, C.P. Cullen, B. Anasori, E. Long, S.-H. Park, A. Seral-Ascaso, A. Shmeliov, D. Krishnan, C. Morant, X. Liu, G.S. Duesberg, Y. Gogotsi, V. Nicolosi, Oxidation Stability of Colloidal Two-Dimensional Titanium Carbides (MXenes), Chemistry of Materials, 29 (2017) 4848-4856.
[34] T. Habib, X. Zhao, S.A. Shah, Y. Chen, W. Sun, H. An, J.L. Lutkenhaus, M. Radovic, M.J. Green, Oxidation stability of Ti 3 C 2 T x MXene nanosheets in solvents and composite films, npj 2D Materials and Applications, 3 (2019) 8.
[35] O. Mashtalir, K.M. Cook, V. Mochalin, M. Crowe, M.W. Barsoum, Y. Gogotsi, Dye adsorption and decomposition on two-dimensional titanium carbide in aqueous media, Journal of Materials Chemistry A, 2 (2014) 14334-14338.
[36] X. Hu, C. Chen, D. Zhang, Y. Xue, Kinetics, isotherm and chemical speciation analysis of Hg (II) adsorption over oxygen-containing MXene adsorbent, Chemosphere, 278 (2021) 130206.

[37] A. Shahzad, K. Rasool, J. Iqbal, J. Jang, Y. Lim, B. Kim, J.-M. Oh, D.S. Lee, MXsorption of mercury: Exceptional reductive behavior of titanium carbide/carbonitride MXenes, Environmental Research, 205 (2022) 112532.
[38] Z. Othman, H.R. Mackey, K.A. Mahmoud, A critical overview of MXenes adsorption behavior toward heavy metals, Chemosphere, (2022) 133849.
[39] K. Li, G. Zou, T. Jiao, R. Xing, L. Zhang, J. Zhou, Q. Zhang, Q. Peng, Self-assembled MXene-based nanocomposites via layer-by-layer strategy for elevated adsorption capacities, Colloids and Surfaces A: Physicochemical and Engineering Aspects, 553 (2018) 105-113.
[40] A. Shahzad, J. Jang, S.-R. Lim, D.S. Lee, Unique selectivity and rapid uptake of molybdenum-disulfide-functionalized MXene nanocomposite for mercury adsorption, Environmental research, 182 (2020) 109005.
[41] S. Laki, A.A. Shamsabadi, F. Alimohammadi, B. Anasori, M. Soroush, Room-Temperature Synthesis of Carboxylated-Mxene Nanosheets for Mercury Scavenging, in: 2019 AIChE Annual Meeting, AIChE, 2019.
[42] P. Zhang, L. Wang, K. Du, S. Wang, Z. Huang, L. Yuan, Z. Li, H. Wang, L. Zheng, Z. Chai, Effective removal of U (VI) and Eu (III) by carboxyl functionalized MXene nanosheets, Journal of hazardous materials, 396 (2020) 122731.
[43] A. Iqbal, J. Hong, T.Y. Ko, C.M. Koo, Improving oxidation stability of 2D MXenes: synthesis, storage media, and conditions, Nano Convergence, 8 (2021) 1-22.
[44] M.J. Ahmed, M. Alam, A rapid spectrophotometric method for the determination of mercury in environmental, biological, soil and plant samples using diphenylthiocarbazone, Spectroscopy, 17 (2003) 45-52.
[45] M. Naguib, O. Mashtalir, J. Carle, V. Presser, J. Lu, L. Hultman, Y. Gogotsi, M.W. Barsoum, Two-dimensional transition metal carbides, ACS nano, 6 (2012) 1322-1331.
[46] B. Anasori, M.R. Lukatskaya, Y. Gogotsi, 2D metal carbides and nitrides (MXenes) for energy storage, Nature Reviews Materials, 2 (2017) 16098.
[47] M. Alhabeb, K. Maleski, B. Anasori, P. Lelyukh, L. Clark, S. Sin, Y. Gogotsi, Guidelines for Synthesis and Processing of Two-Dimensional Titanium Carbide (Ti3C2T x MXene), Chemistry of Materials, 29 (2017) 7633-7644.
[48] M. Ghidiu, J. Halim, S. Kota, D. Bish, Y. Gogotsi, M.W. Barsoum, Ion-exchange and cation solvation reactions in Ti3C2 MXene, Chemistry of Materials, 28 (2016) 3507-3514.
[49] B. Anasori, M.R. Lukatskaya, Y. Gogotsi, 2D metal carbides and nitrides (MXenes) for energy storage, Nature Reviews Materials, 2 (2017) 16098.
[50] Y. Dong, D. Sang, C. He, X. Sheng, L. Lei, Mxene/alginate composites for lead and copper ion removal from aqueous solutions, RSC Advances, 9 (2019) 29015-29022.
[51] A.A. Shamsabadi, F. Seidi, E. Salehi, M. Nozari, A. Rahimpour, M. Soroush, Efficient CO 2-removal using novel mixed-matrix membranes with modified TiO 2 nanoparticles, Journal of Materials Chemistry A, 5 (2017) 4011-4025.
[52] M. Seredych, C.E. Shuck, D. Pinto, M. Alhabeb, E. Precetti, G. Deysher, B. Anasori, N. Kurra, Y. Gogotsi, High-Temperature Behavior and Surface Chemistry of Carbide MXenes Studied by Thermal Analysis, Chemistry of Materials, 31 (2019) 3324-3332.
[53] R.M. McDaniel, M.S. Carey, O.R. Wilson, M.W. Barsoum, A.J. Magenau, Well-Dispersed Nanocomposites Using Covalently Modified, Multilayer, 2D Titanium Carbide (MXene) and In-Situ "Click" Polymerization, Chemistry of Materials, 33 (2021) 1648-1656.
[54] C. He, B. Shen, J. Chen, J. Cai, Adsorption and oxidation of elemental mercury over Ce-MnO x/Ti-PILCs, Environmental science & technology, 48 (2014) 7891-7898.
[55] B. Sun, X. Dong, H. Li, Y. Shang, Y. Zhang, F. Hu, S. Gu, Y. Wu, T. Gao, G. Zhou, Surface charge engineering for two-dimensional Ti2CTx MXene for highly efficient and selective removal of cationic dye from aqueous solution, Separation and Purification Technology, 272 (2021) 118964.
[56] Z. Chen, Y. Liang, D. Jia, W. Chen, Z. Cui, X. Wang, Layered silicate RUB-15 for efficient removal of UO 2 2+ and heavy metal ions by ion-exchange, Environmental Science: Nano, 4 (2017) 1851-1858.

[57] G. Huang, B. Ghalei, A. Pournaghshband Isfahani, H.E. Karahan, D. Terada, D. Qin, C. Li, M. Tsujimoto, D. Yamaguchi, K. Sugimoto, Overcoming humidity-induced swelling of graphene oxide-based hydrogen membranes using charge-compensating nanodiamonds, Nature Energy, 6 (2021) 1176-1187.
[58] A. Sarycheva, T. Makaryan, K. Maleski, E. Satheeshkumar, A. Melikyan, H. Minassian, M. Yoshimura, Y. Gogotsi, Two-dimensional titanium carbide (MXene) as surface-enhanced Raman scattering substrate, The Journal of Physical Chemistry C, 121 (2017) 19983-19988.
[59] E. Satheeshkumar, T. Makaryan, A. Melikyan, H. Minassian, Y. Gogotsi, M. Yoshimura, One-step solution processing of Ag, Au and Pd@ MXene hybrids for SERS, Scientific reports, 6 (2016) 32049.
[60] Y. Singhbabu, K. Sahu, D. Dadhich, A. Pramanick, T. Mishra, R.K. Sahu, Capsule-embedded reduced graphene oxide: synthesis, mechanism and electrical properties, Journal of Materials Chemistry C, 1 (2013) 958-966.
[61] K. Hantanasirisakul, M. Alhabeb, A. Lipatov, K. Maleski, B. Anasori, P. Salles, C. Ieosakulrat, P. Pakawatpanurut, A. Sinitskii, S.J. May, Effects of Synthesis and Processing on Optoelectronic Properties of Titanium Carbonitride MXene, Chemistry of Materials, 31 (2019) 2941-2951.
[62] Z. Guo, X. Zhang, Y. Kang, J. Zhang, Biomass-Derived Carbon Sorbents for Cd(II) Removal: Activation and Adsorption Mechanism, ACS Sustainable Chemistry & Engineering, 5 (2017) 4103-4109.
[63] X. Li, G. Zhang, X. Bai, X. Sun, X. Wang, E. Wang, H. Dai, Highly conducting graphene sheets and Langmuir–Blodgett films, Nature nanotechnology, 3 (2008) 538.
[64] C.-J. Shih, S. Lin, R. Sharma, M.S. Strano, D. Blankschtein, Understanding the pH-dependent behavior of graphene oxide aqueous solutions: a comparative experimental and molecular dynamics simulation study, Langmuir, 28 (2011) 235-241.
[65] Y. Yang, X. Yang, L. Liang, Y. Gao, H. Cheng, X. Li, M. Zou, R. Ma, Q. Yuan, X. Duan, Large-area graphene-nanomesh/carbon-nanotube hybrid membranes for ionic and molecular nanofiltration, Science, 364 (2019) 1057-1062.
[66] D.D. Do, Adsorption analysis: equilibria and kinetics, Imperial college press London, 1998.
[67] N. Huang, L. Zhai, H. Xu, D. Jiang, Stable covalent organic frameworks for exceptional mercury removal from aqueous solutions, Journal of the American Chemical Society, 139 (2017) 2428-2434.
[68] Y. Shin, G.E. Fryxell, W. Um, K. Parker, S.V. Mattigod, R. Skaggs, Sulfur-functionalized mesoporous carbon, Advanced Functional Materials, 17 (2007) 2897-2901.
[69] D.T. Sun, L. Peng, W.S. Reeder, S.M. Moosavi, D. Tiana, D.K. Britt, E. Oveisi, W.L. Queen, Rapid, selective heavy metal removal from water by a metal–organic framework/polydopamine composite, ACS central science, 4 (2018) 349-356.
[70] L. Merí-Bofí, S. Royuela, F. Zamora, M.L. Ruiz-González, J.L. Segura, R. Muñoz-Olivas, M.J. Mancheño, Thiol grafted imine-based covalent organic frameworks for water remediation through selective removal of Hg (II), Journal of Materials Chemistry A, 5 (2017) 17973-17981.
[71] S. Ahmed, J. Brockgreitens, K. Xu, A. Abbas, A nanoselenium sponge for instantaneous mercury removal to undetectable levels, Advanced Functional Materials, 27 (2017) 1606572.
[72] Q. Sun, B. Aguila, J. Perman, L.D. Earl, C.W. Abney, Y. Cheng, H. Wei, N. Nguyen, L. Wojtas, S. Ma, Postsynthetically modified covalent organic frameworks for efficient and effective mercury removal, Journal of the American Chemical Society, 139 (2017) 2786-2793.
[73] B. Li, Y. Zhang, D. Ma, Z. Shi, S. Ma, Mercury nano-trap for effective and efficient removal of mercury (II) from aqueous solution, Nature communications, 5 (2014) 1-7.
[74] N.D. Rudd, H. Wang, E.M. Fuentes-Fernandez, S.J. Teat, F. Chen, G. Hall, Y.J. Chabal, J. Li, Highly efficient luminescent metal–organic framework for the simultaneous detection and removal of heavy metals from water, ACS applied materials & interfaces, 8 (2016) 30294-30303.
[75] W. Yantasee, C.L. Warner, T. Sangvanich, R.S. Addleman, T.G. Carter, R.J. Wiacek, G.E. Fryxell, C. Timchalk, M.G. Warner, Removal of heavy metals from aqueous systems with thiol functionalized superparamagnetic nanoparticles, Environmental science & technology, 41 (2007) 5114-5119.

[76] M.J. Manos, V.G. Petkov, M.G. Kanatzidis, H2xMnxSn3-xS6 (x= 0.11–0.25): A Novel Reusable Sorbent for Highly Specific Mercury Capture Under Extreme pH Conditions, Advanced functional materials, 19 (2009) 1087-1092.
[77] F.J. Alguacil, F.A. López, Adsorption processing for the removal of toxic Hg (II) from liquid effluents: advances in the 2019 year, Metals, 10 (2020) 412.
[78] Z. Hassanzadeh Fard, S.M. Islam, M.G. Kanatzidis, Porous amorphous chalcogenides as selective adsorbents for heavy metals, Chemistry of Materials, 27 (2015) 6189-6192.
[79] J. Ali, H. Wang, J. Ifthikar, A. Khan, T. Wang, K. Zhan, A. Shahzad, Z. Chen, Z. Chen, Efficient, stable and selective adsorption of heavy metals by thio-functionalized layered double hydroxide in diverse types of water, Chemical Engineering Journal, 332 (2018) 387-397.
[80] F. Di Natale, A. Erto, A. Lancia, D. Musmarra, Mercury adsorption on granular activated carbon in aqueous solutions containing nitrates and chlorides, Journal of hazardous materials, 192 (2011) 1842-1850.
[81] N. Ngatijo, D.I. Permatasari, R. Bemis, H. Heriyanti, R. Basuki, Y.G. Wibowo, Decontamination of Mercury from Mined Soil using Magnetite Functionalized Quaternary Ammonium Silica (Fe3O4/SAK), Jurnal Presipitasi: Media Komunikasi dan Pengembangan Teknik Lingkungan, 18 88-98.
[82] https://www.epa.gov/hw/user-friendly-reference-document-hazardous-waste-characteristics.
[83] G.L. Dotto, J.M.N. Santos, I.L. Rodrigues, R. Rosa, F.A. Pavan, E.C. Lima, Adsorption of Methylene Blue by ultrasonic surface modified chitin, Journal of Colloid and Interface Science, 446 (2015) 133-140.
[84] D. An, X. Sun, X. Cheng, L. Cui, X. Zhang, Y. Zhao, Y. Dong, Investigation on mercury removal and recovery based on enhanced adsorption by activated coke, Journal of Hazardous Materials, 384 (2020) 121354.
[85] R. Qu, M. Wang, R. Song, C. Sun, Y. Zhang, X. Sun, C. Ji, C. Wang, P. Yin, Adsorption kinetics and isotherms of Ag (I) and Hg (II) onto silica gel with functional groups of hydroxyl-or amino-terminated polyamines, Journal of Chemical & Engineering Data, 56 (2011) 1982-1990.
[86] X. Zhong, Z. Lu, W. Liang, B. Hu, The magnetic covalent organic framework as a platform for high-performance extraction of Cr (VI) and bisphenol a from aqueous solution, Journal of hazardous materials, 393 (2020) 122353.
[87] F. Liu, S. Hua, C. Wang, M. Qiu, L. Jin, B. Hu, Adsorption and reduction of Cr (VI) from aqueous solution using cost-effective caffeic acid functionalized corn starch, Chemosphere, 279 (2021) 130539.
[88] C.J. Madadrang, H.Y. Kim, G. Gao, N. Wang, J. Zhu, H. Feng, M. Gorring, M.L. Kasner, S. Hou, Adsorption behavior of EDTA-graphene oxide for Pb (II) removal, ACS applied materials & interfaces, 4 (2012) 1186-1193.
[89] M. Wu, R. Kempaiah, P.-J.J. Huang, V. Maheshwari, J. Liu, Adsorption and desorption of DNA on graphene oxide studied by fluorescently labeled oligonucleotides, Langmuir, 27 (2011) 2731-2738.
[90] I. Shibi, T. Anirudhan, Synthesis, characterization, and application as a mercury (II) sorbent of banana stalk (musa paradisiaca)− polyacrylamide grafted copolymer bearing carboxyl groups, Industrial & engineering chemistry research, 41 (2002) 5341-5352.
[91] Q. Zeng, L. Hu, H. Zhong, Z. He, W. Sun, D. Xiong, Efficient removal of Hg2+ from aqueous solution by a novel composite of nano humboldtine decorated almandine (NHDA): Ion exchange, reducing-oxidation and adsorption, Journal of Hazardous Materials, 404 (2021) 124035.
[92] D.W. Smith, Ionic hydration enthalpies, Journal of Chemical Education, 54 (1977) 540.
[93] P. Zhao, M. Jian, Q. Zhang, R. Xu, R. Liu, X. Zhang, H. Liu, A new paradigm of ultrathin 2D nanomaterial adsorbents in aqueous media: graphene and GO, MoS 2, MXenes, and 2D MOFs, Journal of Materials Chemistry A, 7 (2019) 16598-16621.
[94] T. Dudev, C. Lim, Monodentate versus bidentate carboxylate binding in magnesium and calcium proteins: what are the basic principles?, The Journal of Physical Chemistry B, 108 (2004) 4546-4557.
[95] X. Gao, Y. Zhou, Y. Tan, Z. Cheng, B. Yang, Y. Ma, Z. Shen, J. Jia, Exploring adsorption behavior and oxidation mechanism of mercury on monolayer Ti2CO2 (MXenes) from first principles, Applied Surface Science, 464 (2019) 53-60.

[96] X. Wang, S.-M. Bak, M. Han, C.E. Shuck, C. McHugh, K. Li, J. Li, J. Tang, Y. Gogotsi, Surface Redox Pseudocapacitance of Partially Oxidized Titanium Carbide MXene in Water-in-Salt Electrolyte, ACS Energy Letters, 7 (2021) 30-35.
[97] B. Ledesma, S. Román, A. Álvarez-Murillo, E. Sabio, J. González, Cyclic adsorption/thermal regeneration of activated carbons, Journal of analytical and applied pyrolysis, 106 (2014) 112-117.
[98] Z. Qu, J. Xie, H. Xu, W. Chen, N. Yan, Regenerable sorbent with a high capacity for elemental mercury removal and recycling from the simulated flue gas at a low temperature, Energy & Fuels, 29 (2015) 6187-6196.